

Article

Present-Day Geothermal Regime and Thermal Evolution of the Fukang Sag in the Junggar Basin, Northwest China

Huajun Guo ¹, Chenxing Li ^{2,3} , Bo Peng ¹, Xiang Shan ¹, Jiabo Xu ^{2,3}, Ze Zhang ^{2,3} and Jian Chang ^{2,3,*}

¹ PetroChina Hangzhou Research Institute of Geology, Hangzhou 310023, China; guohj_hz@petrochina.com.cn (H.G.)

² National Key Laboratory of Petroleum Resources and Engineering, China University of Petroleum, Beijing 102249, China; lichenxing2020@163.com (C.L.)

³ College of Geosciences, China University of Petroleum, Beijing 102249, China

* Correspondence: changjian@cup.edu.cn; Tel.: +86-0108-9733-332

Abstract: The Fukang Sag in the Junggar Basin is an important petroleum exploration and exploitation region. However, the geothermal regime and tectono-thermal evolution of the Fukang Sag, which control its hydrocarbon generation and conservation, are still controversial. This study involved a systematic analysis of the present-day geothermal gradient, heat flow, and thermal history of the Fukang Sag for better further exploration. According to the well log data and well-testing temperature data, we calculated that the geothermal gradient of the Fukang Sag ranges from 16.6 °C/km to 29.6 °C/km, with an average of 20.8 °C/km, and the heat flow ranges from 34.6 mWm⁻² to 64.3 mWm⁻², with an average of 44.6 mWm⁻². Due to the basement relief, they decrease from northeast to southwest. The weight averages of the single-grain apatite (U-Th)/He ages of the core samples are 1.3–85.2 Ma, and their apatite fission track ages range from 50.9 Ma to 193.8 Ma. The thermal modeling results revealed that the Fukang Sag experienced late Permian, late Jurassic, and late Cretaceous cooling events (although the timing and magnitude of these events varied among the samples), which were related to the continuous compression of the Junggar Basin. In addition, basin modeling indicated that the heat flow of the Fukang Sag decreased from 80 mWm⁻² in the Carboniferous to the current value of 44.6 mWm⁻². The Fukang Sag's edge exhibits prolific hydrocarbon generation in the Carboniferous–Permian source rocks, while the Jurassic source rocks within the sag also undergo abundant hydrocarbon generation. This study provides new insights into the present-day geothermal field and tectono-thermal evolutionary history of the Fukang Sag, which are significant in terms of regional tectonic evolution and oil and gas resource assessment.

Keywords: Fukang Sag; geothermal gradient; heat flow; thermochronometry; thermal history; tectono-thermal evolution; maturity evolution



Citation: Guo, H.; Li, C.; Peng, B.; Shan, X.; Xu, J.; Zhang, Z.; Chang, J. Present-Day Geothermal Regime and Thermal Evolution of the Fukang Sag in the Junggar Basin, Northwest China. *Minerals* **2024**, *14*, 260. <https://doi.org/10.3390/min14030260>

Academic Editor: Luca Aldega

Received: 6 December 2023

Revised: 23 February 2024

Accepted: 27 February 2024

Published: 29 February 2024



Copyright: © 2024 by the authors. Licensee MDPI, Basel, Switzerland. This article is an open access article distributed under the terms and conditions of the Creative Commons Attribution (CC BY) license (<https://creativecommons.org/licenses/by/4.0/>).

1. Introduction

The Junggar Basin, which has an area of 38×10^4 km², is located in Northwest China (Figure 1a) and characterized by abundant oil and gas resources. The previously discovered oil and gas fields are mainly distributed in the uplift areas in the Junggar Basin [1]. In recent years, some new oil and gas fields, which are characterized by lithologic reservoirs [2], were found in the depression areas of the Junggar Basin [3], such as the Mahu Sag, Fukang Sag, Shawan Sag, etc. The Fukang Sag in the central Junggar Basin represents a good exploration prospect along with the discovery of the KT1 oil well (Figure 1c) [4].

The geothermal regime and tectono-thermal evolution in the sedimentary basins are the crucial factors that affect generation and accumulation [5–7]. They can be studied based on borehole temperature data, rock thermal property parameters, thermal indicators, and thermodynamic models [8–10]. The Junggar Basin was considered to be a ‘cool’ basin with a current mean geothermal gradient of ~21 °C/km [11,12]. However, due to insufficient

borehole temperature data, the present-day geothermal characteristics of the Fukang Sag are still controversial. Previous studies discussed the tectono-thermal evolution of the secondary tectonic units of the Junggar Basin, including the Central Depression, Luliang Uplift, Southern Overthrust Belt, etc. [13–18], but there is little research on the tectono-thermal evolution of the Fukang Sag with the combination of apatite fission track (AFT), apatite (U-Th)/He (AHe), and vitrinite reflectance (Ro) data [9].

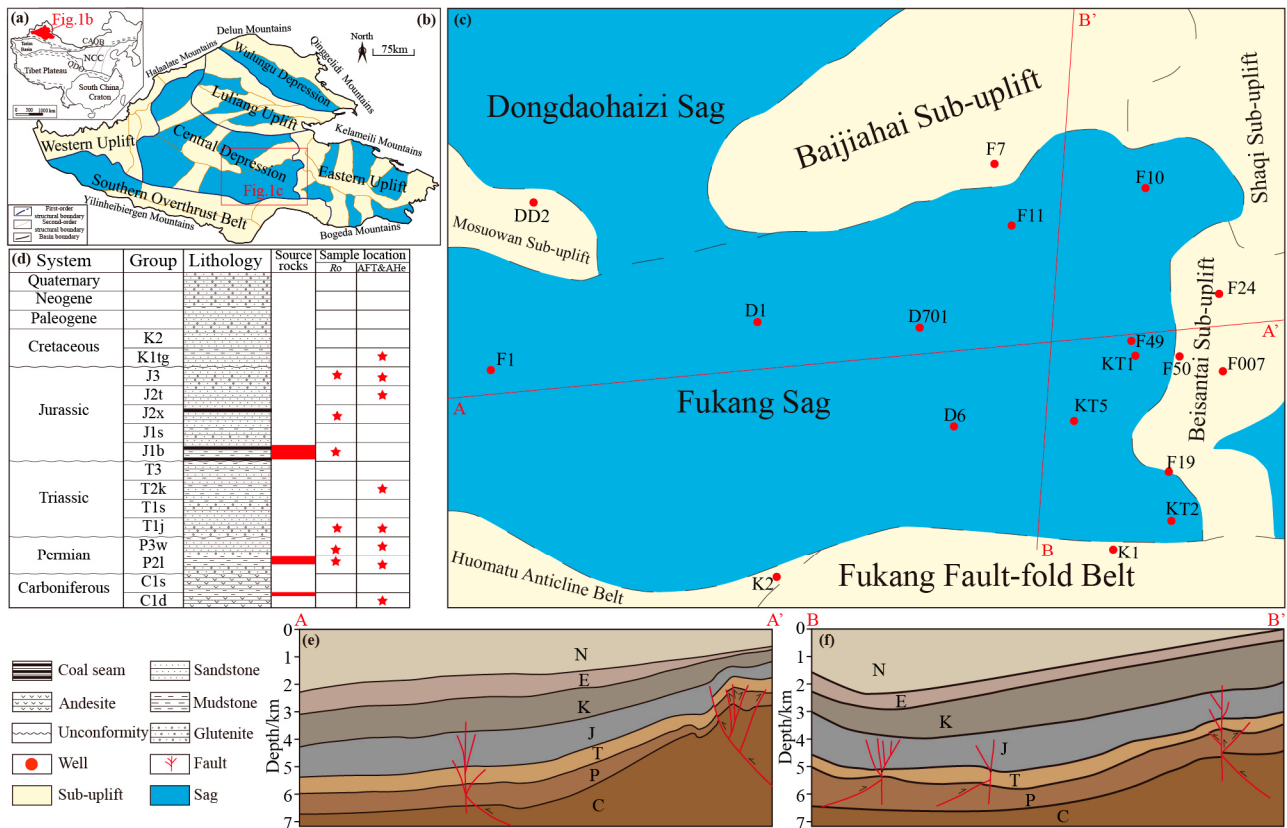


Figure 1. (a) Tectonic framework of China illustrating the location of the Junggar Basin [19]; (b) sketch of the tectonic unit divisions in the Junggar Basin [20]; (c) tectonic units of the Fukang Sag; (d) generalized stratigraphic column and the sample location (the red asterisk symbol) of the Fukang Sag [4]; (e,f) geologic cross sections of the Fukang Sag (the letters N, E, K, J, T, P, and C in the figure are the Neogene, Paleogene, Cretaceous, Jurassic, Triassic, Permian, and Carboniferous formations, respectively) [21], and the AA' and BB' represent the locations of geologic cross sections in the figure (c).

The purpose of this study is to analyze the geothermal regime, reconstruct the thermal history, and further investigate the maturity evolution of source rocks in the Fukang Sag. Firstly, we calculated the present-day geothermal gradients and heat flow using a heat conduction equation and further analyzed the distribution characteristics of the geo-thermal regime. Secondly, the tectono-thermal history of the Fukang Sag was reconstructed with the AFT, AHe, and Ro as thermal indicators. Finally, this study analyzed the maturation evolutionary history of the Carboniferous, Permian, and Jurassic source rocks in the Fukang Sag and its surrounding areas and discussed its effect on hydrocarbon generation and conservation. This study provides new insights into the Fukang Sag’s present-day geothermal regime and tectono-thermal history and is of significance to understanding the tectonic evolution and the evaluation of resources in the Fukang Sag within the Junggar Basin.

2. Geological Setting

The Junggar Basin, located in Northwestern China, is a superimposed basin formed during the Carboniferous [20]. It is bounded by the Halaalate mountains to the west, the

Qinggelidi and Delun Mountains to the north, the Kelameili and Bogeda mountains to the east, and the Yilinheibergen Mountains to the south. The Junggar Basin can be divided into six secondary tectonic units, including the Central Depression, Wulungu Uplift, Luliang Uplift, Eastern Uplift, Western Uplift, and Southern Overthrust Belt (Figure 1b). The Fukang Sag, as the studied area, is a part of the Central Depression bordered by the Southern Overthrust Belt to the south, the Baijiahai Sub-uplift to the north, the Beisantai Sub-uplift to the east, and the Mosuowan Sub-uplift to the west (Figure 1c) [1,3]. Due to multiple tectonic movements, the Fukang Sag developed several unconformities (Figure 1d). The thickness of sedimentary strata in the Fukang Sag is variable. It is thin from west (~7000 m thickness) to east (~3000 m thickness) (Figure 1e). The central Fukang Sag has a thickness of ~6500 m, while the northern Fukang Sag has a thickness of 5000 m (Figure 1f) [21–23].

Due to the variation in the sedimentary environment, the lithology in the Fukang Sag is unique for each stratum. The Carboniferous strata are predominantly composed of volcanic rocks such as andesite [22]. During the Permian, the Fukang Sag developed a lake–river delta and deposited sandstone, mudstone, and glutenite. The Triassic stratum in the Fukang Sag consists of mudstone and sandstone. During the Jurassic, the Fukang Sag developed a riverine and a lacustrine braided river delta, and deposited sandstone and mudstone with coal-bearing layers [24]. Since the Cretaceous, the Fukang Sag has predominantly deposited sandstone and glutenite. The Carboniferous Dishuiquan Formation (C₁d), Permian Lucaogou Formation (P₂l), and Jurassic Badaowan Formation (J₁b) are good source rocks [2] (Figure 1d), which provided massive amounts of hydrocarbon for the discovered oil and gas fields in the Fukang Sag and its surrounding areas [23].

3. Present-Day Geothermal Regime

The present geothermal regime represents the final state of thermal evolution in a sedimentary basin, so it is a necessary constraint for simulating tectono-thermal history [8,25]. The present-day geothermal regime of one sedimentary basin can be studied based on measured borehole temperature data [26,27]. In this study, we collected the well log data of 13 wells and well-testing temperature data of >50 wells. The well log data, which were obtained by measuring the temperature at intervals of 200 m from top to bottom for one borehole after the completion of drilling and recovery of formation temperatures, reflect the variations in the geothermal gradient with depth (Figure 2a). The well-testing temperature is equal to the burial temperature of the oil-producing formations (Figure 2b).

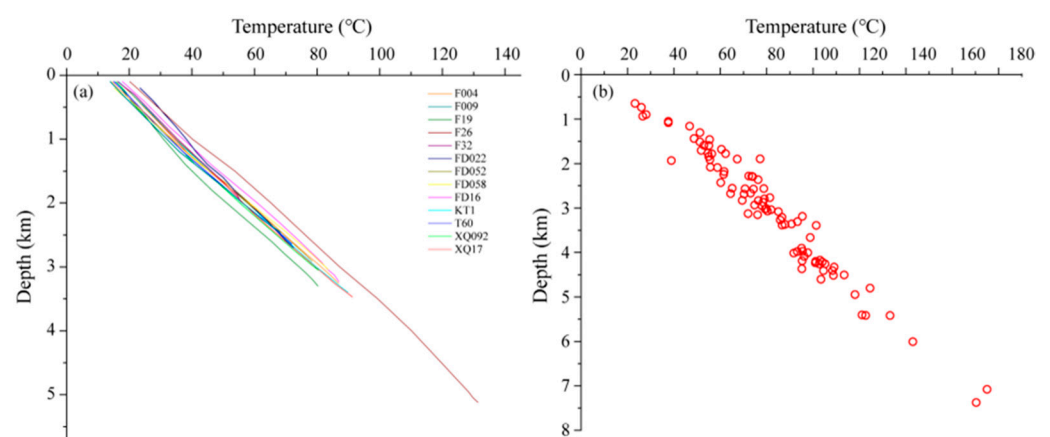


Figure 2. Relationship between temperature and depth in the Fukang Sag. (a) Well log data and (b) well-testing temperature data of boreholes.

3.1. Calculation Method

In this study, the present-day geothermal gradient and heat flow of the Fukang Sag were calculated based on the collected borehole temperature data and rock thermal property

parameters. Meanwhile, their spatial distribution characteristics and relevant influencing factors were analyzed.

Due to the differential rock thermal conductivity, the deep geothermal gradient in sedimentary basins is usually smaller than the shallow geothermal gradient. Therefore, the variation in the temperature depths across different boreholes can make it difficult to correctly reveal the spatial distribution of the actual geothermal gradients for a basin. To resolve this problem, this study referred to the unified depth method provided by Chang et al. to study the geothermal gradient of the Fukang Sag [27]. First, we calculated the burial temperature at the depths of 4000 m for all the wells in the Fukang Sag with a one-dimensional steady-state heat conduction equation (Equation (1)):

$$T_i^b = T_i^t + \frac{(q_i^t \times Z_i)}{K_i} - \frac{(A_i \times Z_i^2)}{(2 \times K_i)} \quad (1)$$

where i is the structural layer number; T_i^b and T_i^t are the temperatures of the bottom and top surfaces in the structural layer i , respectively; Z_i is the thickness of structural layer (in km); A_i is the rock heat production rate (μWm^{-3}); K_i is the rock thermal conductivity ($\text{W}/(\text{m}\cdot\text{K})$) [11]; and q_i^t is the heat flow of the top of the structural layer i (mWm^{-2}).

Then, the geothermal gradient at unified depths of 0–4000 m could be calculated with Equation (2):

$$G_{4000} = \frac{T_Z - T_0}{Z - Z_0} \quad (2)$$

where G_{4000} is the average geothermal gradient ($^\circ\text{C}/\text{km}$), T_Z is the temperature at depths of 4000 m, T_0 is the constant temperature near the surface ($14\text{ }^\circ\text{C}$), Z is the depth of the temperature measurement (in km), and Z_0 is the depth of the constant temperature zone (0.02 km).

The surface heat flow represents the energy flux through the Earth's surface. It is equal to the rock thermal conductivity times the geothermal gradient (Equation (3)):

$$q_s = -K_t \times \frac{dT}{dZ} \quad (3)$$

where q_s is the surface heat flow (mWm^{-2}), K_t is the harmonic mean thermal conductivity ($\text{W}/(\text{m}\cdot\text{K})$), and dT/dZ is the geothermal gradient ($^\circ\text{C}/\text{km}$).

When the geothermal gradient and heat flow of each well in the Fukang Sag were obtained, we could analyze their spatial distribution characteristics with the Kriging method [28].

3.2. Present-Day Geothermal Gradient and Heat Flow

The geothermal gradients in the Fukang Sag and its surrounding areas at depths 0–4000 m range from 16.6 to 29.6 $^\circ\text{C}/\text{km}$, with an average of 20.8 $^\circ\text{C}/\text{km}$, indicating obvious variation among the different tectonic units (Figure 3). In the Fukang Sag, the geothermal gradient ranges from 17.2 to 27.6 $^\circ\text{C}/\text{km}$, with an average geothermal gradient of 20.3 $^\circ\text{C}/\text{km}$, showing that it gradually increases from southwest to northeast. The average geothermal gradients of the Baijiahai Sub-uplift and Beisantai Sub-uplift in the northeast of the Fukang Sag are 23.0 $^\circ\text{C}/\text{km}$ and 22.7 $^\circ\text{C}/\text{km}$, respectively, and exhibit similar spatial distribution characteristics. Generally, the geothermal gradients in the uplift areas are larger than those in the depression areas. In addition, the geothermal gradients in the Fukang Fault-fold Belt just range from 16.6 $^\circ\text{C}/\text{km}$ to 21.3 $^\circ\text{C}/\text{km}$, with an average value of 18.8 $^\circ\text{C}/\text{km}$, which is very low and related to low thermal conductivity of the sedimentary cover [11,29–31].

The heat flow in the Fukang Sag ranges from 34.6 mWm^{-2} to 64.3 mWm^{-2} , with an average value of 44.6 mWm^{-2} , indicating an obvious decrease from northeast to southwest (Figure 4). The Shaqi Sub-uplift exhibits the highest heat flow, which ranges from

51.6 mWm^{-2} to 64.3 mWm^{-2} , with an average value of 54.1 mWm^{-2} . The Baijiahai and Beisantai Sub-uplifts also show relatively high heat flow, with average values of 47.8 mWm^{-2} and 47.9 mWm^{-2} , respectively. The heat flow in the Fukang Sag is lower than in the uplift areas and ranges from 38.27 mWm^{-2} to 55.2 mWm^{-2} , with an average of 44.13 mWm^{-2} . The Fukang Fault-fold Belt shows the lowest heat flow, with an average value of only 40.3 mWm^{-2} . Generally, the heat flow spatial distribution in the Fukang Sag and its surrounding areas is related to the basement relief (Figure 1e,f).

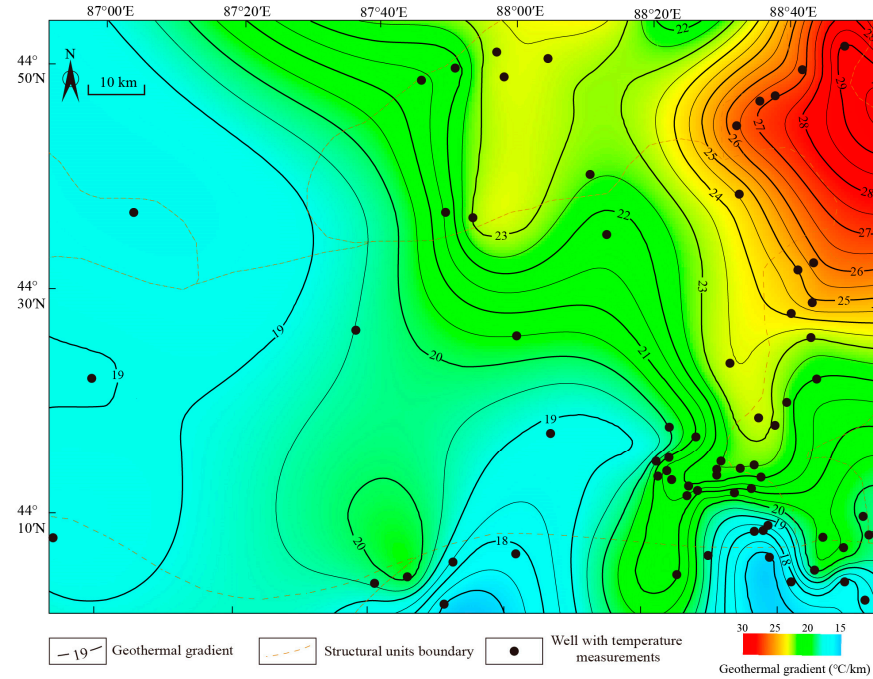


Figure 3. Distribution pattern of present-day geothermal gradient of the Fukang Sag with uniform depths of 0–4000 m.

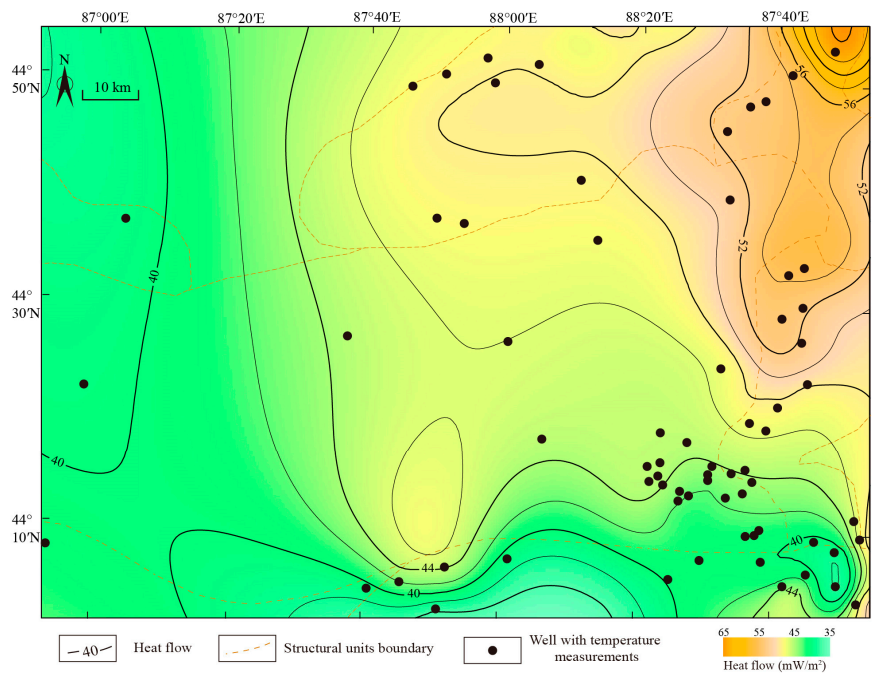


Figure 4. Distribution pattern of present-day heat flow of the Fukang Sag.

4. Thermal History

4.1. Sampling Strategy and Results

In this study, we collected 20 samples from the drilling wells F19, F49, F50, KT2, KT5, and K2 for studying the tectono-thermal history of the Fukang Sag (Tables 1 and 2; Figure 1c,d). The apatite grains for AFT and AHe dating were separated from the sandstone samples using conventional mineral separation techniques. The measurement procedures for the AFT and AHe ages were introduced in reference [32]. The vitrinite reflectance (Ro) for the mudstone samples was measured under an optical microscope equipped with a spectrophotometer [33].

Table 1. The apatite fission track data of the samples in the Fukang Sag.

Sample	Depth (m) (Fm.)	No. Grains	ρ_s ($10^5/\text{cm}^2$) (Ns ¹)	U (ppm) ₂	P (χ^2) ³	Central Age $\pm 2\sigma$ (Ma)	Mean Track Length $\pm 2\sigma$ (μm) (n ⁴)	Dpar ⁵ (μm)
F191	1865 (K1tg)	27	6.84 (763)	9.48	0.12	143.3 \pm 13.4	13.2 \pm 1.9 (42)	2.12 (1.25–3.07)
F192	2674 (T1j)	33	7.76 (1499)	7.71	0.2	193.8 \pm 12.2	13.1 \pm 1.5 (53)	2.24 (1.75–3.32)
F193	2981 (C)	6	3.52 (60)	10.46	0.09	95.7 \pm 45.8	13.9 (1)	2.11 (1.36–2.52)
F491	5020 (T1j)	26	1.20 (163)	4.37	0.14	50.9 \pm 9.4	—	2.11 (1.57–2.77)
F501	4288 (P3w)	11	2.50 (121)	3.20	0.31	156.0 \pm 37.5	—	2.34 (1.63–2.89)
F502	4378 (P2l)	25	1.95 (190)	4.60	0.84	82.8 \pm 12.0	12.2 \pm 0.9 (8)	2.31 (1.73–2.86)
K21	2593 (J3)	18	8.80 (568)	10.06	0.2	139.2 \pm 16.8	11.4 \pm 1.6 (20)	2.30 (1.79–2.75)
K22	3250 (J2t)	3	2.21 (17)	3.38	0.28	129.4 \pm 73.1	—	2.71 (2.36–2.96)
KT21	3676 (T2k)	26	6.89 (1023)	6.88	0.17	189.4 \pm 14.4	11.9 \pm 1.9 (24)	2.20 (1.68–2.74)
KT22	4292 (P3w)	12	5.02 (336)	6.65	0.35	161.6 \pm 18.2	11.7 \pm 0.8 (11)	2.58 (1.75–3.48)

¹ Ns: sum of spontaneous fission tracks for one sample. ² U (ppm): uranium content value obtained from the LA-ICP-MS measurement. ³ P (χ^2): chi-square probability. ⁴ n: the number of confined fission tracks. ⁵ Dpar: the mean maximum diameter of etch figures parallel to the c-axis, which was used as a kinetic parameter.

Table 2. The vitrinite reflectance data of the wells in the Fukang Sag.

Well Number	Sample Depth (m)	Formation	Vitrinite Reflectance (%)
KT2	4602.32	P3w	0.74
	4867.11	P2l	0.83
KT5	6189.46	P2l	1.16
	6246.90	P2l	1.21
F50	4288.85	P3w	0.84
	4326.72	P3w	0.97
	4374.84	P2l	0.75
F49	5623.97	P2l	0.91
	5626.64	P2l	1.01
	5629.21	P2l	1.03

The samples from the wells F19, F49, F50, K2, and KT2 show the variant AFT and AHe ages (Tables 1 and 3, Figures 5 and 6), recording the differential thermal histories in the Fukang Sag. The measured central AFT ages range from 50.9 Ma to 193.8 Ma, younger than their corresponding stratigraphic ages. There is a negative correlation between the AFT ages and the depths, except for the samples F191 and F192 from the Well F19 (Table 1), which indicated that a higher temperature results in much more annealing. The AHe weighted mean ages range from 1.29 Ma to 85.2 Ma. Most of the single-grain AHe ages are younger than their corresponding stratigraphic ages (Table 3). There is a negative correlation between single-grain AHe ages and effective uranium concentration (Figure 6b) and no correlation between single-grain AHe ages and radius (Figure 6a), indicating that the dispersion of the single-grain AHe ages is related to radiation damage. Despite the intense radiation damage, some single-grain AHe ages are still older than the corresponding stratigraphic age (for the sample F191). The measured Ro data range from 0.74% to 1.21% (Table 2), indicating that the source rocks has reached the middle–late mature stage.

Table 3. The apatite (U-Th)/He data of the samples in the Fukang Sag.

Sample	Grain No.	Rs ² (μm)	Mass (μg)	He (ncc)	U (ppm)	Th (ppm)	Th/U	eU ¹ (ppm)	Raw Age (Ma)	FT ³	Corrected Age ± 1σ (Ma)	Weight Mean Age ± 1σ (Ma) ⁴
F191	1	92.8	19.31	0.2908	0.60	1.60	2.66	0.98	126.32	0.84	149.7 ± 4.04	85.2 ± 0.71
	2	50.3	3.16	0.0357	0.61	4.93	8.07	1.79	52.41	0.72	72.5 ± 0.77	
	3	59.8	5.83	0.2151	3.02	6.80	2.25	4.66	65.61	0.76	86.0 ± 11.31	
	4	43.3	3.01	0.2203	1.59	14.74	9.29	5.13	118.52	0.68	175.3 ± 2.29	
F192	1	71.2	10.94	0.4150	1.31	6.33	4.84	2.83	111.14	0.80	139.1 ± 3.09	2.52 ± 0.19
	2	66.6	7.80	0.0120	8.71	8.60	0.99	10.78	1.19	0.82	1.4 ± 0.19	
	3	71.7	11.01	0.0500	0.73	3.49	4.75	1.57	24.02	0.83	29.0 ± 1.38	
F193	1	61.1	4.84	0.0226	0.55	4.17	7.62	1.55	25.11	0.77	32.8 ± 0.54	38.26 ± 0.37
	2	53.4	3.29	0.0107	0.22	2.75	12.41	0.88	30.91	0.74	42.0 ± 0.52	
	3	120.3	42.19	0.4664	0.62	1.88	3.02	1.08	85.02	0.88	96.8 ± 7.36	
	4	71.0	8.46	0.3446	1.09	4.00	3.68	2.05	163.9	0.80	205.9 ± 6.46	
F501	1	45.6	2.37	0.0160	2.27	13.01	5.74	5.39	10.46	0.70	15.0 ± 0.50	6.29 ± 0.05
	2	63.0	6.38	0.0229	3.01	11.14	3.70	5.68	5.25	0.77	6.8 ± 0.28	
	3	67.8	7.47	0.0051	0.44	3.82	8.71	1.35	4.18	0.79	5.3 ± 0.09	
	4	51.8	3.96	0.0058	0.51	8.29	16.37	2.50	4.89	0.73	6.7 ± 0.07	
F491	1	53.0	3.96	0.0039	0.72	4.58	6.40	1.82	4.56	0.74	6.2 ± 0.05	3.86 ± 0.01
	2	62.3	6.49	0.0055	0.99	4.94	4.97	2.18	3.26	0.77	4.2 ± 0.03	
	3	98.0	22.13	0.0134	0.97	3.45	3.58	1.79	2.82	0.85	3.3 ± 0.02	
	4	56.1	4.22	0.0059	0.52	4.47	8.67	1.59	7.32	0.75	9.8 ± 0.16	
K22	1	51.4	3.32	0.0060	1.56	9.58	6.15	3.86	3.91	0.78	5.0 ± 1.25	8.44 ± 0.89
	2	49.1	3.25	0.0850	8.31	4.22	0.51	9.32	23.23	0.76	30.6 ± 2.32	
	3	45.5	2.32	0.0040	2.56	9.08	3.54	4.74	3.03	0.75	4.0 ± 1.51	
K21	1	53.5	4.25	0.0183	0.53	5.01	9.46	1.73	20.73	0.74	28.1 ± 0.25	1.65 ± 0.11
	2	75.4	10.47	0.0152	9.62	14.45	1.50	13.09	0.92	0.81	1.1 ± 0.12	
	3	72.2	8.70	0.0810	1.81	5.86	3.23	3.22	24.07	0.80	30.0 ± 1.32	
	4	68.1	7.94	0.0601	12.38	32.70	2.64	20.23	3.11	0.79	3.9 ± 0.34	
KT21	1	64.3	7.08	0.1554	1.69	10.41	6.15	4.19	43.56	0.78	56.0 ± 1.03	1.29 ± 0.04
	2	53.0	4.11	0.2969	2.98	16.35	5.49	6.90	86.84	0.73	118.3 ± 2.37	
	3	56.8	5.30	0.3676	2.29	16.45	7.19	6.24	92.36	0.75	123.1 ± 3.45	
	4	54.4	4.03	0.0091	14.01	32.06	2.29	21.70	0.86	0.74	1.2 ± 0.04	
KT22	1	81.8	12.56	0.0030	0.46	2.40	5.22	1.03	1.92	0.87	2.2 ± 0.74	15.18 ± 0.14
	2	64.5	6.16	0.0030	0.39	2.67	6.93	1.03	3.96	0.78	5.1 ± 1.69	
	3	55.0	4.41	0.0075	0.30	3.79	12.72	1.21	11.74	0.74	15.8 ± 0.15	

¹ eU: effective uranium content, $eU = U + 0.235 \times Th$ [34]. ² Rs: radius of a sphere with an equivalent surface area-to-volume ratio to the cylindrical crystals [35]. ³ FT: the α -ejection correction [32]. ⁴ Weighted mean age with 95% confidence is calculated in the IsoplotR [36].

4.2. Thermal History Inversion

The partial annealing zone (PAZ) of AFT dating is considered to be between 60 °C and 125 °C [37]. The AHe partial retention zone (PRZ) is 40~80 °C [38]. By integrating AFT and AHe data in the thermal history simulation process, it is possible to reveal a thermal history of 40–125 °C. The thermal history modeling in this study was carried out by the HeFTy v1.9.1 software with Monte Carlo models [39–41]. When modeling the time–temperature paths, some geological constraints need to be inputted. We set the start time of each sample to be the corresponding stratigraphic ages and the starting temperature (at surface) to be 14 °C [42]. The present-day burial temperature was calculated based on the present-day geothermal gradient and sample depth in the Fukang Sag. The temperature changes in the thermal history were related to the tectonic evolution of the Fukang Sag. Therefore, we set a series of constraints for the possible timing of tectonic movements based on the unconformities (Figure 7).

The AFT and AHe data were modeled by using a multi-kinetic annealing model and an apatite radiation damage accumulation and annealing model, respectively [39,41]. The green region in the figures represents an ‘acceptable’ path range ($0.05 \leq GOF < 0.5$), the purple region represents a ‘good’ path range ($0.5 \leq GOF \leq 1.0$) (Figure 7), and the thick black line represents the best path.

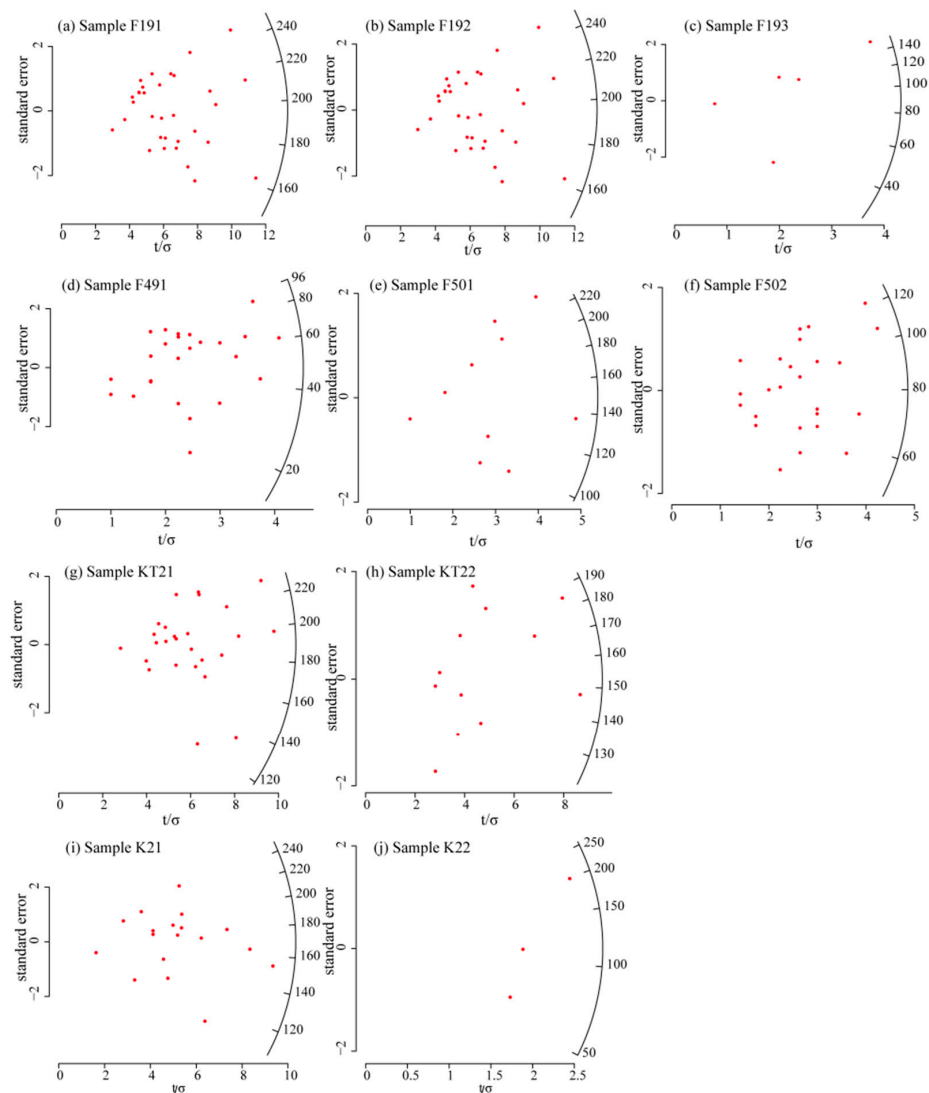


Figure 5. Radial plots of the AFT ages. The red dots represent the single-grain age of the samples.

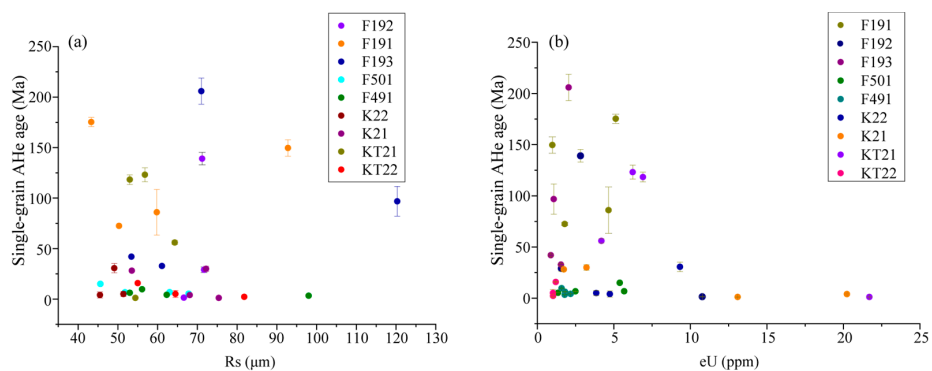


Figure 6. Correlation of single-grain AHe age with R_s (a) and eU (b) for the samples from the Fukang Sag.

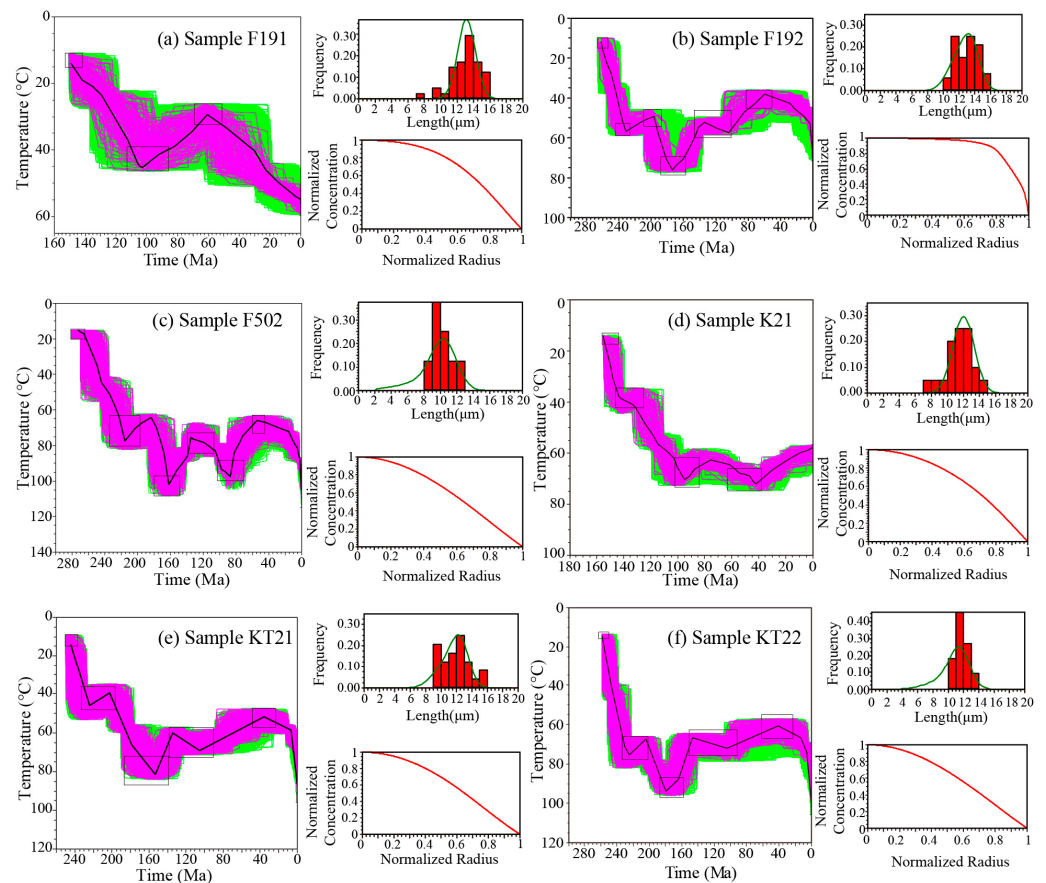


Figure 7. Thermal histories of the samples F191, F192, F502, K21, KT21, and KT22. The green lines are ‘acceptable’ time–temperature paths. The purple lines are ‘good’ time–temperature paths. And the black line is the best time–temperature path. The figures show the simulated and measured c-axis projected fission track length data and AHe data with the best time–temperature path.

The thermal history of the Permian sample F192 revealed that the Beisantai Sub-uplift has experienced three cooling events of 240 Ma–200 Ma, 165 Ma–140 Ma, and 100 Ma–60 Ma since the late Permian, while that of the lower Cretaceous sample F191 just revealed a late Cretaceous (100 Ma–60 Ma) cooling event (Figure 7a,b). The thermal histories of the sample F502 indicated that the northeast margin of the Fukang Sag experienced three cooling events, which occurred in 220 Ma–190 Ma, 160 Ma–140 Ma, and 90 Ma–40 Ma (Figure 7c). And the thermal histories of the samples KT21 and KT22 in the southeast margin of the Fukang Sag also recorded three cooling events of ~230 Ma–200 Ma, 165 Ma–150 Ma, and 100 Ma–40 Ma (Figure 7e,f). The sample K21 from well K2 in the southern margin of the Fukang Sag just record two cooling events of 100 Ma–80 Ma and 40 Ma–0 Ma (Figure 7d).

4.3. Paleo-Heat Flow Simulation

The paleo-heat flow evolutionary histories of the Fukang Sag can be modeled by combining the burial histories of the studied wells, the measured R_o , and the t-T paths of the samples mentioned above. The 1D burial and thermal histories of the studied wells were reconstructed based on the stratigraphic thickness and the erosion amounts using Basinmod 1D software [43] with the Easy% R_o model [33]. The erosion amounts were equal to the temperature difference for one cooling event revealed by the time–temperature paths of the samples divided by the geothermal gradient (Figure 7). After the burial history was rebuilt, the thermal modeling constraints, including present-day heat flow, rock thermal conductivity, and R_o data, were input. Then, we iteratively modified the paleo-heat flow to ensure that the simulated thermal history in Basinmod was consistent with the time–

temperature paths obtained from the samples of the AFT and AHe simulations, and the simulated Ro path overlapped with the measured Ro data (Figure 8).

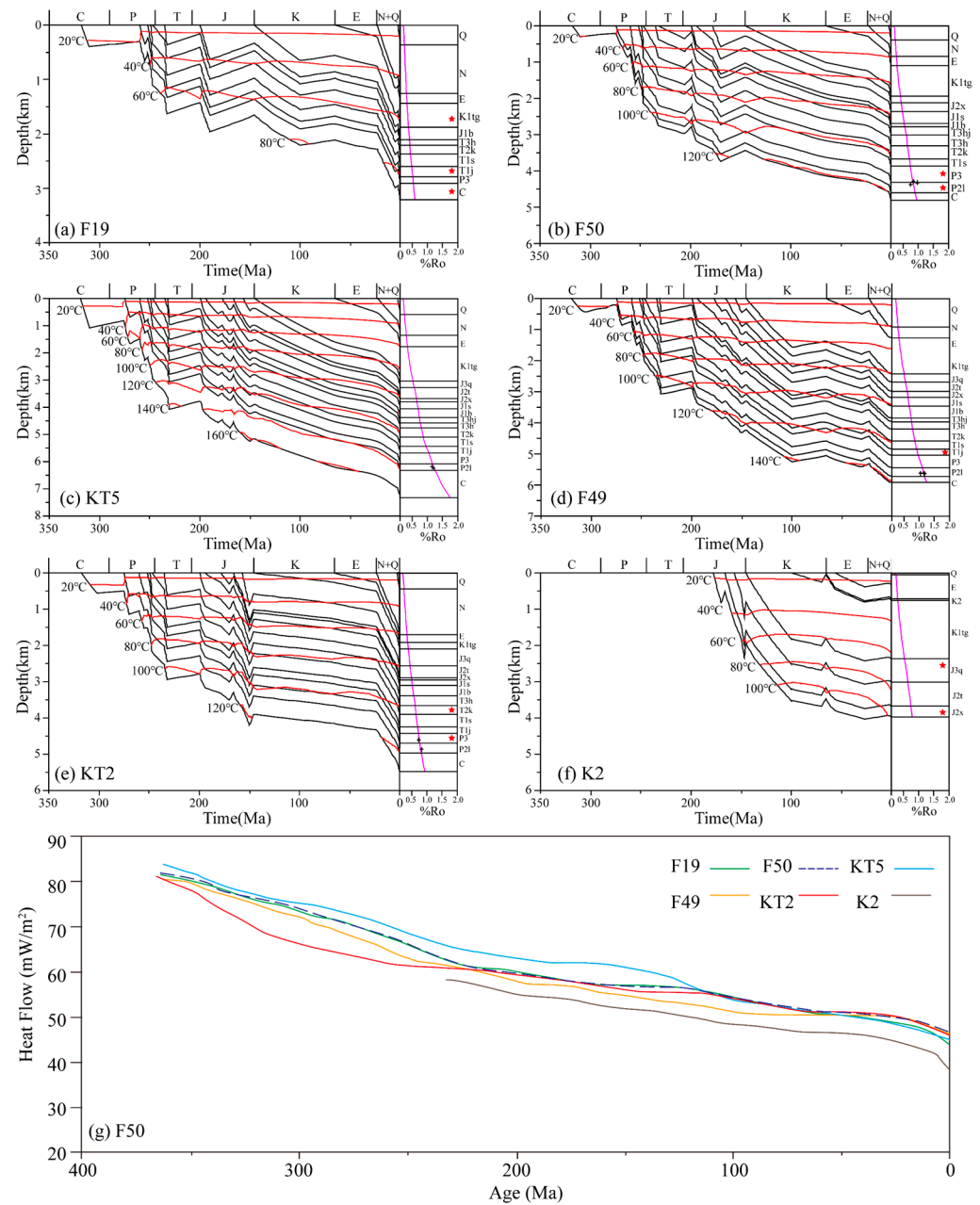


Figure 8. The burial–thermal history (a–f) and the paleo-heat flow evolution (g) in wells F19, F49, F50, KT2, KT5, and K2. The purple curve represents the simulated %Ro data. The black daggers are the measured %Ro data, and the asterisk symbol indicate the samples’ layers with AFT and AHe data.

The paleo-heat flow of the Fukang Sag has gradually decreased since the Carboniferous (Figure 8). The paleo-heat flow was 75–85 mWm^{−2} in the early Carboniferous. And it decreased to 60–70 mWm^{−2} from the Carboniferous to the Permian. Due to the stress field transition from extension to compression, the paleo-heat flow began slowly decreasing during the Triassic and Jurassic and was 55–65 mWm^{−2} by the end of the Jurassic. Due to the differential deposition in the early Cretaceous [44], the paleo-heat flow among the studied wells in the Fukang Sag experienced different evolutionary histories. During the late Cretaceous, the paleo-heat flow in the Fukang Sag decreased to 50–60 mWm^{−2}. The

rapid sedimentation during the Cenozoic caused the paleo-heat flow of the Fukang Sag to decrease to $\sim 45 \text{ mWm}^{-2}$ [12].

5. Discussion

5.1. Geothermal Controlling Factors in the Fukang Sag

The heat flow in the Fukang Sag and its surrounding area ranges from 34.55 to 64.31 mWm^{-2} , which is lower than that in sedimentary basins in Central and Eastern China and offshore areas [45–47], as well as the average heat flow in continental regions [48]. The present-day geothermal regime in the Fukang Sag should be related to the long-term stable tectonic environment [49]. A previous study indicated that the crustal structure, tectonic evolution, basement relief, subsurface fluid activity, and rock heat production play an important effect on the present-day geothermal regime of basins [50]. In this study, we discuss how the basement relief and tectonic evolution affect the geothermal regime of the Fukang Sag.

The basement of the Junggar Basin consists of lower Carboniferous strata [51]. The Beisantai, Shaqi, and Baijiahai Sub-uplifts show very shallow basements with burial depths of 3–5 km, while the burial depths of the basement in the Fukang Sag exceeds 6.5 km (Figure 1e,f). This basement relief is in accordance with the distribution of the geothermal regime in the Fukang Sag and its surrounding area. In addition to the basement relief, the present-day geothermal regime of the Fukang Sag is also related to regional tectonic evolution. During the Permian, The Fukang Sag and Beisantai, Shaqi, and Baijiahai Sub-uplifts formed due to N-S striking compression [20,52]. These areas always kept a shallow basement with thin sedimentary layers. Before the Jurassic, the areas in the southern part of the Fukang Sag were at the deposition center and deposited relatively thick sediments [44,52]. Along with the uplifting of the Tianshan from the late Jurassic to early Cretaceous, the deposition center migrated northward to the Fukang Sag [23]. During the Cenozoic, a thrust-and-fold belt formed in the south of the Fukang Sag with intense N-S striking compression, causing uplift and erosion [53]. Although the southern part of the Fukang Sag stays in a structurally elevated position right now, the existing thick sediments still make it relatively cool.

The geothermal gradient and heat flow in the shallow basement areas are usually higher those that in the deep basement areas. This phenomenon is attributed to the “thermal refraction” effect caused by the differential rock thermal conductivities between the bedrock and sedimentary rocks [54], which resulted in heat accumulation in the uplift areas. It also confirms that basins developed in a compressional regime, which had thicker sedimentary rocks, exhibit lower heat flow than basins developed in a stretching regime [55].

5.2. Differential Maturation Evolution of Source Rocks

Exploration indicates that the Jurassic and overlying formations in the Beisantai, Baijiahai, and Shaqi uplifts are rich in oil and gas resources [56], which came from the Carboniferous, Permian, and Jurassic source rocks in the Fukang Sag [4,56]. For a better understanding the hydrocarbon generation and accumulation process, this study discussed the maturation evolutionary process of the source rocks in the Fukang Sag, including the Carboniferous Dishuiquan Formation (C_1d), Permian Lucaogou Formation (P_2l), and Jurassic Badaowan Formation (J_1b) (Figure 9).

Due to the very low burial temperature throughout geological time, the Jurassic source rock in the well F19 area is currently immature, with a R_o value of $\sim 0.3\%$, and the Carboniferous source rock in the Well F19 area just reached the early maturity stage in the late Cretaceous and probably began generating oil. In the well F50 area, the Jurassic source rock is also currently immature, while the Carboniferous and Permian source rocks reached the early and middle maturity stages in the early Triassic and the early Jurassic, respectively. In the well KT2 area, the Jurassic source rock entered the early maturity stage during the late Cenozoic, and the Carboniferous and Permian source rocks reached the early and middle maturity stages in the early Triassic and the late Jurassic, respectively. The

Jurassic source rock in the Fukang Sag (well F49 and KT5 areas) entered the early maturity stage in the early Cretaceous, while the Carboniferous and Permian source rocks reached the early, middle, and late maturity stages in the early Triassic, late Triassic, and Cretaceous, respectively. Due to the thick sediments developed by the long-term deposition, the current Ro values of the Carboniferous and Permian source rocks in the F49 and KT5 wells range from 1.1% to 1.3%. Generally, the differential maturity of the source rocks in the Fukang Sag is related to burial depth.

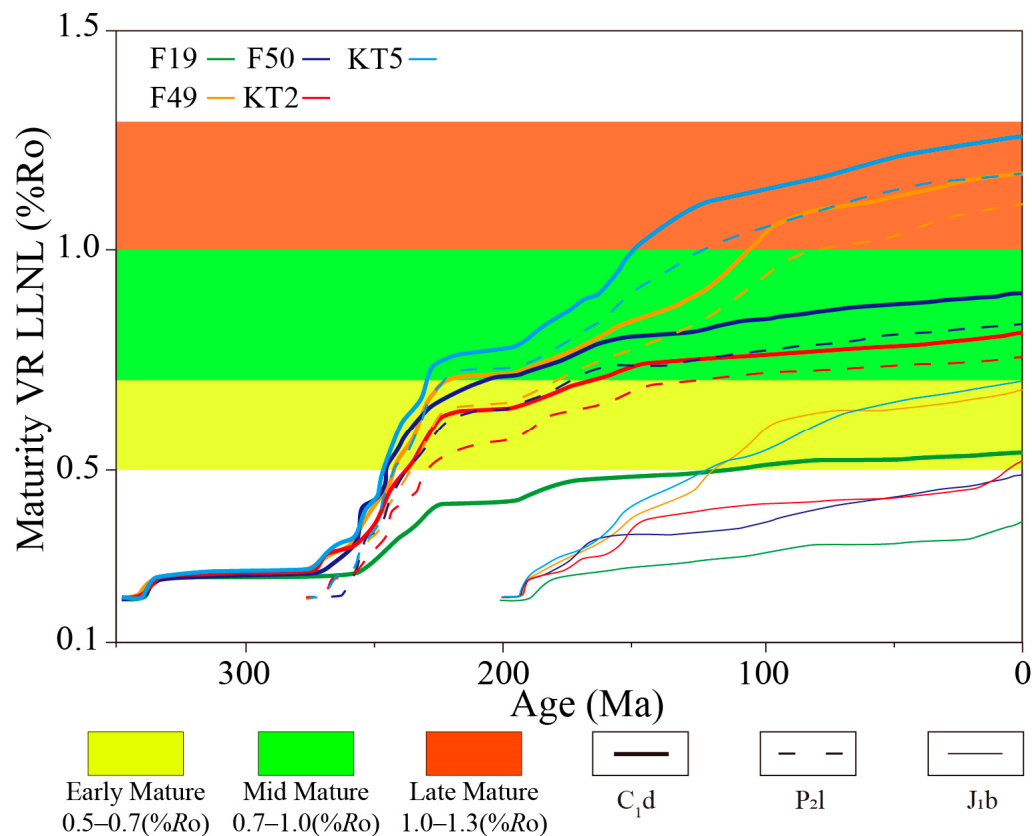


Figure 9. The maturation evolutionary histories of the source rocks in the Fukang Sag. The thicker solid line, dashed line, and thinner solid line represent C_{1d}, P_{2l}, and J_{1b} source rocks, respectively.

The Carboniferous and Permian source rocks along the east margin of the Fukang Sag began generating oil in the late Triassic, which should provide massive amounts of oil for the peripheral oil fields. This suggests that Carboniferous and Permian source rocks in the central region of Fukang Sag had higher maturity, possibly resulting in gas generation. According to the geochemical data, the oil and gas reservoirs in the uplift areas of the Fukang Sag belonged to a mixed source [57]. Our study supports that liquid oil primarily originated from the margin of the Fukang Sag, while gas originated from the center of the Fukang Sag [58].

6. Conclusions

In this study, we comprehensively used borehole temperature data, AFT data, AHe data, and Ro data to investigate the geothermal regime and tectono-thermal history of the Fukang Sag in the Junggar Basin. The present-day average geothermal gradient and heat flow in the Fukang Sag are 20.8 °C/km and 44.6 mWm⁻², respectively. Due to the basement relief, they decrease from northeast to southwest. The AFT and AHe ages range between 50.9 Ma–193.8 Ma and 1.3 Ma–85.2 Ma, respectively. Thermal history simulation revealed three cooling events in the late Permian, late Jurassic, and late Cretaceous periods. In addition, the basin modeling results also indicated that the paleo-heat flow of the

Fukang Sag decreased from 80 mWm⁻² in the Carboniferous to the current value of 44.6 mWm⁻². The Carboniferous–Permian source rocks in the eastern Fukang Sag entered into the middle–late maturation stage during the late Triassic, showing great potential for oil generation.

Author Contributions: Conceptualization, H.G. and J.C.; methodology, C.L. and B.P.; software, C.L. and J.X.; validation, B.P., X.S. and C.L.; formal analysis, J.C.; investigation, C.L.; resources, B.P. and X.S.; data curation, Z.Z.; writing—original draft preparation, C.L.; writing—review and editing, J.C. and H.G.; visualization, B.P.; project administration, J.C.; funding acquisition, H.G. All authors have read and agreed to the published version of the manuscript.

Funding: This research was funded by the China National Petroleum Corporation’s “Fourteenth Five Year Plan” Basic Prospective Major Scientific and Technological Projects (No. 2021DJ0202 and No. 2021DJ0108) and the China National Petroleum Corporation’s Important Science and Technology Project (No. 2023ZZ24-01).

Data Availability Statement: The data are contained within the article.

Conflicts of Interest: Huajun Guo, Bo Peng, and Xiang Shan are employees of PetroChina Hangzhou Research Institute of Geology. The paper reflects the views of the scientists and not the company.

References

1. He, W.; Fei, L.; Ablimiti, Y.; Yang, H.; Lan, W.; Ding, J.; Bao, H.; Guo, W. Accumulation conditions of deep hydrocarbon and exploration potential analysis in Junggar Basin, NW China. *Earth Sci. Front.* **2019**, *26*, 189–201. [\[CrossRef\]](#)
2. Tao, S.; Yuan, X.; Hou, L.; Zhang, G.; Yang, F.; Tao, X.; Wei, Y.; Li, X.; Zhang, C.; Wang, L.; et al. Formation and distribution of large lithologic-stratigraphic oil & gas fields (provinces). *J. Nat. Gas Geosci.* **2018**, *3*, 51–65. [\[CrossRef\]](#)
3. Yang, Z.; Zou, C. “Exploring petroleum inside source kitchen”: Connotation and prospects of source rock oil and gas. *Pet. Explor. Dev.* **2019**, *46*, 181–193. [\[CrossRef\]](#)
4. He, H.Q.; Zhi, D.M.; Tang, Y.; Liu, C.W.; Chen, H.; Guo, X.G.; Wang, Z. A great discovery of Well Kangtan 1 in Fukang Sag in the Junggar Basin and its significance. *China Pet. Explor.* **2021**, *26*, 1–11. [\[CrossRef\]](#)
5. Hu, S.B.; Wang, J.Y. Principles and progresses on thermal regime of sedimentary basins—An overview. *Earth Sci. Front.* **1995**, *2*, 171–180.
6. Zhang, G. Co-control of source and heat: The generation and distribution of hydrocarbons controlled by source rocks and heat. *Acta Pet. Sin.* **2012**, *33*, 723–738. [\[CrossRef\]](#)
7. Ren, Z.; Cui, J.; Qi, K.; Yang, G.; Chen, Z.; Yang, P.; Wang, K. Control effects of temperature and thermal evolution history of deep and ultra-deep layers on hydrocarbon phase state and hydrocarbon generation history. *Nat. Gas Ind. B* **2020**, *7*, 453–461. [\[CrossRef\]](#)
8. Qiu, N.; Chang, J.; Zhu, C.; Liu, W.; Zuo, Y.; Xu, W.; Li, D. Thermal regime of sedimentary basins in the Tarim, upper Yangtze and north China cratons, China. *Earth-Sci. Rev.* **2022**, *224*, 103884. [\[CrossRef\]](#)
9. Qiu, N.; He, L.; Chang, J.; Zhu, C. Research progress and challenges of thermal history reconstruction in sedimentary basins. *Pet. Geol. Exp.* **2020**, *42*, 790–802. [\[CrossRef\]](#)
10. Ren, Z.; Cui, J.; Qi, K.; Yang, P.; Liu, X.; Zhang, C.; Yang, G.; Gao, Y.; Zhang, Y.; Xing, G. New progress in research on theories and methods for reconstruction of deep and ultra—Deep thermal evolution history in superimposed basins. *J. Northwest Univ. (Nat. Sci. Ed.)* **2022**, *52*, 910–929.
11. Rao, S.; Hu, S.B.; Zhu, C.Q.; Tang, X.Y.; Li, W.W.; Wang, J.Y. The characteristics of heat flow and lithospheric thermal structure in Junggar Basin, northwest China. *Chin. J. Geophys.* **2013**, *56*, 2760–2770. [\[CrossRef\]](#)
12. Qiu, Z.; Zhang, Z.; Xu, E. Geothermal regime and Jurassic source rock maturity of the Junggar Basin, northwest China. *J. Asian Earth Sci.* **2008**, *31*, 464–478. [\[CrossRef\]](#)
13. Li, D.; He, D.; Santosh, M.; Ma, D.; Tang, J. Tectonic framework of the northern Junggar Basin part I: The eastern Luliang Uplift and its link with the East Junggar terrane. *Gondwana Res.* **2015**, *27*, 1089–1109. [\[CrossRef\]](#)
14. He, D. Multi-cycle superimposed sedimentary basins in China: Formation, evolution, geologic framework and hydrocarbon occurrence. *Earth Sci. Front.* **2022**, *29*, 24–59. [\[CrossRef\]](#)
15. Zhou, Z.; Pan, C.; Fan, S.; Han, L. Geothermal characteristics of the Junggar Basin and its significance to oil searching. *Xinjiang Pet. Geol.* **1989**, *10*, 67–74.
16. Liu, G.; Zhang, H. The Hydrocarbon Occurrence and Characteristics of Geothermal field in Junggar Basin. *Xinjiang Pet. Geol.* **1992**, *13*, 100–107.
17. Pan, C.; Zhou, Z.; Wang, Q. Study of thermal history of source beds in Junggar basin by apatite fission track. *Oil Gas Geol.* **1989**, *10*, 35–39.
18. Rao, S.; Zhu, Y.K.; Hu, S.B.; Wang, Q. The thermal history of Junggar Basin: Constraints on the tectonic attribute of the Early-Middle Permian basin. *Acta Geol. Sin.* **2018**, *92*, 1176–1195.

19. Zhao, G.C.; Sun, M.; Wilde, S.A.; Li, S.Z. Late Archean to Paleoproterozoic evolution of the North China Craton: Key issues revisited. *Precambrian Res.* **2005**, *136*, 177–202. [[CrossRef](#)]
20. He, D.; Zhai, G.; Kuang, J.; Zhang, Y.; Shi, X. Distribution and tectonic features of paleo-uplifts in the Junggar Basin. *Chin. J. Geol.* **2005**, *40*, 248–261.
21. Ma, C.; Wu, K.Y.; Pei, Y.W.; Li, T.R. Quantitative analysis of tectonic characteristics and evolution in the eastern Junggar Basin. *J. Geomech* **2019**, *25*, 313–323.
22. He, D.F.; Zhang, L.; Wu, S.T.; Li, D.; Zhen, Y. Tectonic evolution stages and features of the Junggar Basin. *Oil Gas Geol.* **2018**, *39*, 845–861.
23. Fang, S.; Guo, Z.; Jia, C.; Zhang, Z.; Wang, X.; Wang, M. Meso-Cenozoic Heavy Minerals' Assemblages in the Southern Junggar Basin and Its Implications for Basin-orogen Pattern. *Chin. J. Geol.* **2006**, *41*, 648–662.
24. Zhu, M.; Yuan, B.; Liang, Z.; Yang, D.; Tang, X. Fault properties and evolution in the periphery of Junggar Basin. *Acta Pet. Sin.* **2021**, *42*, 1163–1173. [[CrossRef](#)]
25. Chang, J.; Qiu, N.; Xu, W. Thermal regime of the Tarim Basin, Northwest China: A review. *Int. Geol. Rev.* **2017**, *59*, 45–61. [[CrossRef](#)]
26. Förster, A. Analysis of borehole temperature data in the Northeast German Basin: Continuous logs versus bottom-hole temperatures. *Pet. Geosci.* **2001**, *7*, 241–254. [[CrossRef](#)]
27. Chang, J.; Qiu, N.-S.; Zhao, X.-Z.; Xu, W.; Xu, Q.-C.; Jin, F.-M.; Han, C.-Y.; Ma, X.-F.; Dong, X.-Y.; Liang, X.-J. Present-day geothermal regime of the Jizhong depression in Bohai Bay basin, East China. *Chin. J. Geophys.* **2016**, *59*, 1003–1016. [[CrossRef](#)]
28. Oliver, M.A.; Webster, R. A tutorial guide to geostatistics: Computing and modelling variograms and kriging. *Catena* **2014**, *113*, 56–69. [[CrossRef](#)]
29. Bullard, E.C. The time necessary for a bore hole to attain temperature equilibrium. *Geophys. J. Int.* **1947**, *5*, 127–130. [[CrossRef](#)]
30. Wang, S.J.; Hu, S.B.; Wang, J.Y. The characteristics of heat flow and geothermal field in Junggar Basin. *Chin. J. Geophys.* **2000**, *43*, 816–824. [[CrossRef](#)]
31. Jin, J.; Liu, M.; Liu, Y.; Wang, J.; Gao, C.; Luo, Z.; Lu, F.; Ren, Y. Present-day temperature-pressure field and its controlling factors of the lower composite reservoir in the southern margin of Junggar Basin. *Chin. J. Geol.* **2021**, *56*, 28–43. [[CrossRef](#)]
32. Chang, J.; Yang, L.; Li, C.; Qiu, N.; Zhang, H.; Wang, X. Tectono-thermal evolution of the northern Tarim Basin, Central Asia: New insights from apatite low-temperature thermochronometers. *J. Asian Earth Sci.* **2004**, *259*, 105919. [[CrossRef](#)]
33. Sweeney, J.J.; Burnham, A.K. Evaluation of a simple model of vitrinite reflectance based on chemical kinetics. *AAPG Bull.* **1990**, *74*, 1559–1570. [[CrossRef](#)]
34. Farley, K.A.; Wolf, R.A.; Silver, L.T. The effects of long alpha-stopping distances on (U-Th)/He ages. *Geochim. Cosmochim. Acta* **1996**, *60*, 4223–4229. [[CrossRef](#)]
35. Shuster, D.L.; Flowers, R.M.; Farley, K.A. The influence of natural radiation damage on helium diffusion kinetics in apatite. *Earth Planet. Sci. Lett.* **2006**, *249*, 148–161. [[CrossRef](#)]
36. Meesters, A.G.C.A.; Dunai, T.J. Solving the production–diffusion equation for finite diffusion domains of various shapes: Part II. Application to cases with α -ejection and nonhomogeneous distribution of the source. *Source. Chem. Geol.* **2002**, *186*, 57–73. [[CrossRef](#)]
37. Vermeesch, P. IsoplotR: A free and open toolbox for geochronology. *Geosci. Front.* **2018**, *9*, 1479–1493. [[CrossRef](#)]
38. Green, P.F.; Duddy, I.R.; Gleadow, A.J.; Tingate, P.R.; Laslett, G.M. Thermal annealing of fission tracks in apatite: 1. A qualitative description. *Chem. Geol. Isot. Geosci. Sect.* **1986**, *59*, 237–253. [[CrossRef](#)]
39. Flowers, R.M.; Ketcham, R.A.; Shuster, D.L.; Farley, K.A. Apatite (U-Th)/He thermochronometry using a radiation damage accumulation and annealing model. *Geochim. Cosmochim. Acta* **2009**, *73*, 2347–2365. [[CrossRef](#)]
40. Nielsen, S.B.; Balling, N. Joint inversion of temperature, vitrinite reflectance and fission tracks in apatite with examples from the eastern North Sea area—Response to discussion. *Basin Res.* **2023**, *35*, 2045–2048. [[CrossRef](#)]
41. Ketcham, R.A.; Carter, A.; Donelick, R.A.; Barbarand, J.; Hurford, A.J. Improved modeling of fission-track annealing in apatite. *Am. Mineral.* **2007**, *92*, 799–810. [[CrossRef](#)]
42. Qiu, N.S.; Ming, Z.; Wang, X.L.; Yang, H.B. Tectono-thermal evolution of the Junggar Basin, NW China: Constraints from Ro and apatite fission track modelling. *Pet. Geosci.* **2005**, *11*, 361–372.
43. Vincent, C.J.; Merriman, R.J. *Thermal Modelling of the Cheshire Basin Using BasinModTM*; British Geological Survey: Nottingham, UK, 2004.
44. Cao, S.; He, D. Evolution of the Caiwopu basin, Xinjiang. *Geotecton. Metallog.* **1997**, *21*, 262–269.
45. Fang, S.H.; Guo, Z.J.; Song, Y.; Wu, C.D.; Zhang, Z.C.; Wang, M.N.; Fan, R.D. Sedimentary facies evolution and basin pattern of the Jurassic in southern margin area of Junggar Basin. *J. Palaeogeogr.* **2005**, *7*, 347–356.
46. Qiu, N.; Kang, Y.; Jing, Z. Temperature and pressure field in the Tertiary succession of the western Qaidam basin, northeast Qinghai-Tibet Plateau, China. *Mar. Pet. Geol.* **2003**, *20*, 493–507. [[CrossRef](#)]
47. Ren, Z.; Zhang, S.; Gao, S.; Cui, J.; Xiao, Y.; Xiao, H. Tectonic thermal history and its significance on the formation of oil and gas accumulation and mineral deposit in Ordos Basin. *Sci. China Ser. D Earth Sci.* **2007**, *50*, 27–38. [[CrossRef](#)]
48. He, L.; Wang, K.; Xiong, L.; Wang, J. Heat flow and thermal history of the South China Sea. *Phys. Earth Planet. Inter.* **2001**, *126*, 211–220. [[CrossRef](#)]

49. Jiang, G.-Z.; Gao, P.; Rao, S.; Zhang, L.-Y.; Tang, X.-Y.; Huang, F.; Zhao, P.; Pang, Z.-H.; He, L.-J.; Hu, S.-B.; et al. Compilation of heat flow data in the continental area of China. *Chin. J. Geophys.* **2016**, *59*, 2892–2910. [[CrossRef](#)]
50. Popov, Y.A.; Pimenov, V.P.; Pevzner, L.A.; Romushkevich, R.A.; Popov, E.Y. Geothermal characteristics of the Vorotilovo deep borehole drilled into the Puchezh-Katunk impact structure. *Tectonophysics* **1998**, *291*, 205–223. [[CrossRef](#)]
51. Wang, X.; Song, Y.; Bian, B.; Zhao, J.; Zhang, H.; Yan, M.; Pei, S.; Xu, Q.; Wang, S.; Liu, H.; et al. Basement structure of the Junggar Basin. *Earth Sci. Front.* **2021**, *28*, 235–255. [[CrossRef](#)]
52. Zheng, M.; Fan, X.; He, W.; Yang, T.; Tang, Y.; Ding, J.; Wu, H.; Chen, L.; Guo, J. Superposition of deep geological structural evolution and hydrocarbon accumulation in the Junggar Basin. *Earth Sci. Front.* **2019**, *26*, 22–32. [[CrossRef](#)]
53. Hendrix, M.S.; Graham, S.A.; Carroll, A.R.; Sobel, E.R.; Mcknight, C.L.; Schulein, B.J.; Wang, Z. Sedimentary record and climatic implications of recurrent deformation in the Tian Shan: Evidence from Mesozoic strata of the north Tarim, south Junggar, and Turpan basins, northwest China. *Geol. Soc. Am. Bull.* **1992**, *104*, 53–79. [[CrossRef](#)]
54. Liu, S.; Lei, X.; Feng, C.; Li, X. Heat flow, deep formation temperature and thermal structure of the Tarim Basin, Northwest China. *Earth Sci. Front.* **2017**, *24*, 41–55.
55. Mckenzie, D. Some remarks on the development of sedimentary basins. *Earth Planet. Sci. Lett.* **1978**, *40*, 25–32. [[CrossRef](#)]
56. Li, Z.; Peng, S. U-Pb geochronological records and provenance system analysis of the Mesozoic-Cenozoic sandstone detrital zircons in the northern and southern piedmonts of Tianshan, Northwest China: Responses to intracontinental basin-range evolution. *Acta Petrol. Sin.* **2013**, *29*, 739–755.
57. Zheng, J.; Xiang, C.; Wang, X.; Lei, D.; Yang, N.; A, B.; Zhang, L.; Zhang, Y.; Wang, L. Characteristics of the Jurassic source rocks and their shale gas exploration potential in the Fukang Sag of the Junggar Basin. *Geol. Rev.* **2015**, *61*, 217–226.
58. Yang, F.; Song, Y.; Chen, H.; Gong, D.; Bian, B.; Liu, H. Evaluation of Carboniferous Songkaersu Formation source rocks and gas-source correlation in the Fukang Sag of eastern Junggar Basin. *Nat. Gas Geosci* **2019**, *30*, 1018–1026.

Disclaimer/Publisher’s Note: The statements, opinions and data contained in all publications are solely those of the individual author(s) and contributor(s) and not of MDPI and/or the editor(s). MDPI and/or the editor(s) disclaim responsibility for any injury to people or property resulting from any ideas, methods, instructions or products referred to in the content.